nature communications

Article

https://doi.org/10.1038/s41467-025-64647-w

Biomimetic strong and tough MXene fibers with synergy between micropores and dual interfaces

Received: 25 February 2025

Accepted: 18 September 2025

Published online: 31 October 2025

Check for updates

Jianfeng Gu[1,5], Donghui Li[1,5], Yichen Ren[2,5], JiaHao Li[3,5], Xinyi Ji[1], Xue Liu[1], Weiqing Zhan[1], Xialian Zhao[1], Quan Wang[3], Xiewen Liu[2], Huihui Wang[1], Xinmin Zhang[1], YinBo Zhu[3] ✉, Zhao Yue[2] ✉, Heng-An Wu[3], Yongsheng Chen[4] & Jiajie Liang[1,4] ✉

Despite high porosity, deer antlers exhibit high strength and toughness from synergistic hierarchical structures. MXene fibers offer promising applications but suffer from poor mechanical properties due to internal voids and weak interfaces. Conventional strengthening removes voids and enhances interlayer interactions, but yields rigid, brittle fibers. Here, we tackle this trade-off by constructing strong and slidable double-interfaces that can cooperate with internal micropores in MXene fibers to mimic the delicate structure of deer antlers. These voids, typically considered defects, instead enhance load-bearing and energy dissipation. At an optimal porosity of ~21%, the MXene fibers achieve high tensile strength, ductility, and toughness of 1060.1 ± 33.5 MPa, 34.2 ± 1.8%, and 136.1 ± 6.5 MJ m^{-3}, respectively. Notably, this MXene-matrixed fiber shows elasticity and high durability and is even softer than polymer fibers, while maintaining an electrical conductivity of over 10500 S cm^{-1} after being coated with silver nanowires. This biomimetic approach enables robust, multifunctional fibers for smart textiles.

Titanium carbide $Ti_3C_2T_x$ (MXene) nanosheets have shown promising applications in various advanced fields due to their exceptional electrical conductivity as well as mechanical and physiochemical properties[1–3]. Recent successes in assembling MXenes into macroscopic fibers have inspired the development of high-performance MXene fiber electronics[4–7]. The hydrophilic surface groups (-OH, -O, and -F) of MXenes allow them to be formed into fibers through simple and scalable solution-based spinning or drawing techniques[5–7]. However, MXene nanosheets with large aspect ratios are easily wrinkled and folded under external stress[4,8]. These uneven features of MXene nanosheets will disrupt the interlayer packing of neighboring sheets and weaken the interlayer interactions. Moreover, the packed MXene nanosheets are facilely to generate thick slabs with drastically increased stiffness, decreasing the packing density of the final lamellar structure. Thus, MXene nanosheets are hard to generate compacted lamellar fibers without interlayer voids[9,10]. The inherent porosity, loose lamellar structure, and intrinsically weak interlayer interactions between MXene nanosheets give their macroscopic fibers poor mechanical properties[4,6,7,11]. Thus, there is a urgent need for strong, tough, and ductile MXene fibers.

Numerous efforts have been made to improve the mechanical strength of MXene fibers by removing internal voids and increasing nanosheet alignment[7,11,12]. For example, MXene fibers with an orientation factor of 0.86 and a tensile strength of 110 MPa were obtained via

[1]School of Materials Science and Engineering, National Institute for Advanced Materials, Nankai University, Tianjin, China. [2]Department of Microelectronics, Nankai University, Tianjin, China. [3]CAS Key Laboratory of Mechanical Behavior and Design of Materials, Department of Modern Mechanics, University of Science and Technology of China, Hefei, China. [4]Key Laboratory of Functional Polymer Materials of Ministry of Education, College of Chemistry, Nankai University, Tianjin, China. [5]These authors contributed equally: Jianfeng Gu, Donghui Li, Yichen Ren, JiaHao Li. ✉e-mail: zhuyinbo@ustc.edu.cn; yuezhao@nankai.edu.cn; liang0909@nankai.edu.cn

wet-spinning using a flat spinneret nozzle[7]. Aligned MXene fibers fabricated from a strengthened gel network showed a porosity of 6.13% and a tensile strength of 343 MPa[11]. However, while reducing voids enhanced the stress-transfer efficiency between MXene nanosheets[1,13], an ultra-compact structure limited the motion of the nanosheets within fibers, resulting in limited ductility and toughness[4,11]. Enhancing interfacial interactions and introducing a shell layer can also address the trade-off between the strength and toughness of MXene fibers[4,12]. For instance, based on the synergy between wet spinning and thermal drawing techniques, an ultra-compact MXene fiber modified with a polymer crosslinker and outer layer was obtained, which achieved a strength of 585.5 MPa and toughness of 66.7 MJ m^{-3}[4]. The formation of interlocks between the outer polymer shell and inner MXene fiber further increased its strength to 707 MPa[12]. Nevertheless, the introduction of a non-functional outer layer has restricted their applications in fiber electronics. We recently introduced a slide-ring crosslinker to form internal-mechanically-interlocked networks between MXene nanosheets to achieve functional MXene fibers with a strength of 502 MPa and a toughness of 59.7 MJ m^{-3}[5]. Despite the numerous attempts to improve the mechanical properties of MXene fibers via interface and structure engineering, they still exhibit inadequate mechanical performance. Their tensile strength lags far behind that of carbon-based fibers[14–16], and their toughness is much lower than that of polymer fibers[17,18].

Deer antlers are a natural bio-composite with a unique combination of high strength and toughness due to the presence of multiple structures[19–21]. The compact bone in antlers is composed of osteons with high-mineralized seams and multiple pores surrounded by concentric lamellae (Fig. 1a)[19,20] that produce a high level of shear strain under load to strengthen the antlers[19]. The interlocking effect from high-mineralized seams induces osteon sliding to deflect propagating cracks, playing a significant role in toughening[20]. In contrast to conventional structural materials, which regard voids as defects that reduce mechanical properties, the multiple pores in deer antlers with unique shapes and preferred orientation can cooperate with surrounding lamellar structures to induce shear deformation and regulate stress distribution. This results in an improved load-bearing and energy-dissipating capacity[19,20,22]. The synergistic regulation of

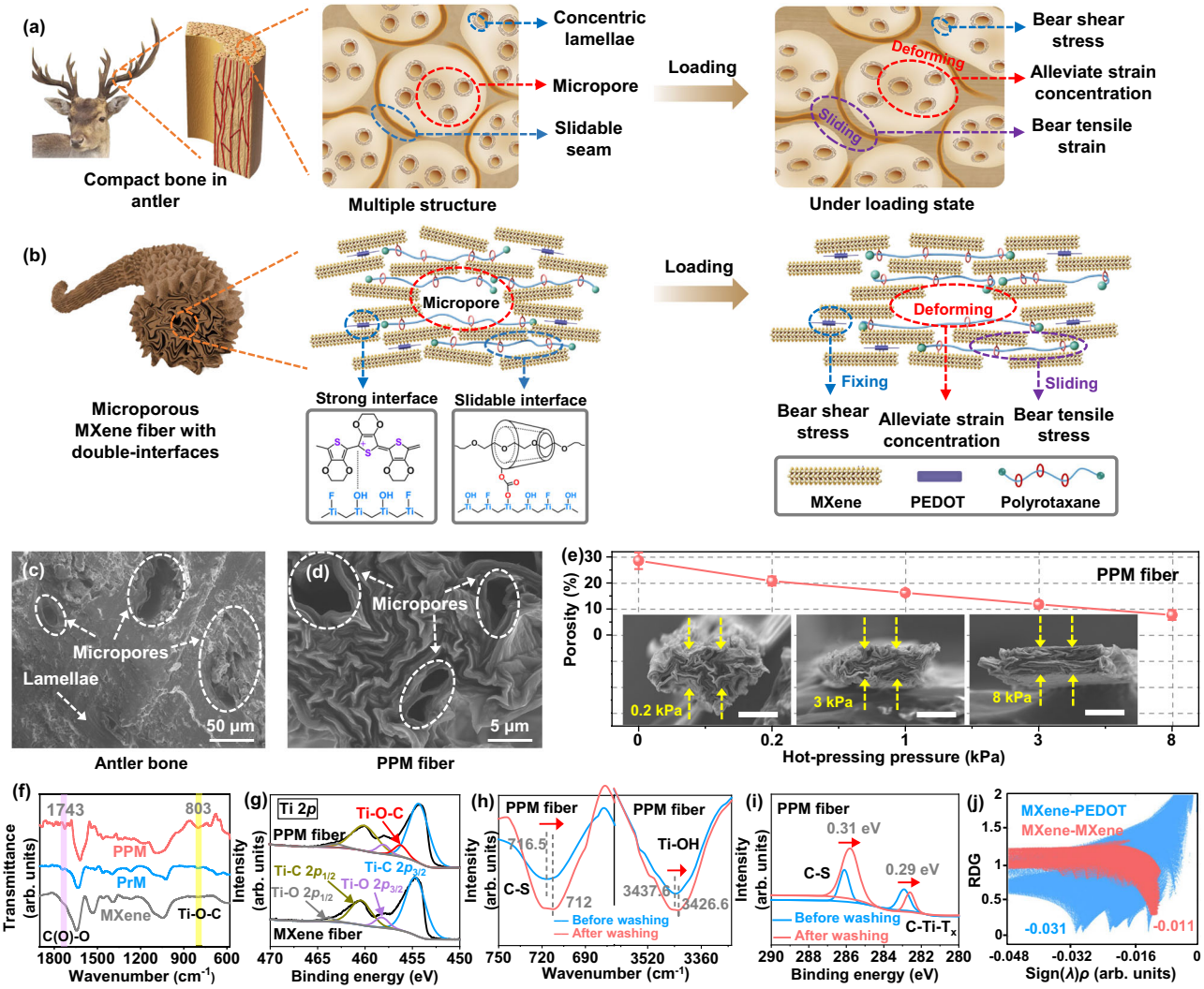

Fig. 1 | Design and characterization of MXene/PEDOT:PSS/polyrotaxane (PPM) fiber. Schematic illustration of the strengthening and toughening structural characteristics of (**a**) deer antlers and (**b**) PPM fibers. Cross-sectional SEM images of (**c**) an anti-plane in deer antlers and (**d**) PPM fibers (repeated independently with similar structures for 5 times). **e** Average porosity of PPM fiber as a function of hot-pressing pressure. Inset showing cross-sectional SEM images of a PPM fiber hot-pressed at 0.2 kPa, 3 kPa, and 8 kPa (repeated independently with similar structures for 5 times). The scale bar is 20 μm. The error bars represent the mean ± standard deviation from n = 5 independent experiments). **f** FT-IR spectra of pure MXene, MXene/polyrotaxane (PrM), and PPM fibers. **g** XPS spectrum of pure MXene and PPM fiber in the Ti 2p region. **h** FT-IR spectra of C-S bonds and Ti-OH groups in PPM fiber before and after washing partial PSS. **i** XPS spectrum of the C 1 s region for PPM fiber before and after washing partial PSS. **j** RDG of MXene-MXene and MXene-PEDOT interfaces.

multiple porous and interfacial structures makes deer antlers one of the toughest and strongest known biological materials[19,20,22]. Thus, mimicking the structural characteristics of deer antlers may inspire the development of strong and tough MXene fibers with inherent micropores.

Herein, we propose a biomimetic strategy involving synergy between double-interface engineering and microporosity modulation to develop ultra-strong and super-tough MXene fibers with unprecedented ductility, elasticity, and softness. We introduced PEDOT to form a strong interface with MXene nanosheets via electrostatic interactions for fiber strengthening, imitating the functions of concentric lamellae in the osteon of deer antlers (Fig. 1b). We crosslinked MXene with a slide-ring polyrotaxane to construct a slidable interface for toughening, mimicking osteon sliding via interlocked seams in deer antlers. Unlike traditional densification strategies that remove voids to form compact structures for material strengthening, we took the opposite approach and retained a high volume of micropores in our MXene fibers. Resembling the porous structure in deer antlers, the micropores softened the MXene fibers and provided room for interface sliding to regulate stress distribution, thus further strengthening and toughening the fibers. As a result, our MXene fibers achieved a milestone tensile strength over 1 GPa and a record-high toughness exceeding 130 MJ m^{-3}, which have never been realized in ultra-compact MXene fibers. Moreover, our MXene fibers were elastic, durable, and soft, making them suitable for textile applications. After wet-coating with a silver nanowire (AgNW) network, the fibers offered an ultrahigh electrical conductivity exceeding 10500 S cm^{-1} without compromising their mechanical properties. These MXene fibers show great potential applications in fiber electronics, such as sensory fibers for smart textiles. MXene-based textiles sensing systems are expected to achieve high-precision measurements in complex multi-physical fields through innovative multi-modal sensing decoupling mechanisms while maintaining excellent wearability[23,24]. This synergistic approach addresses the critical limitations of conventional rigid or coupled sensor designs, paving the way for next-generation smart textiles and wearable devices with enhanced functionality and reliability[25].

Results

Fiber fabrication

MXene fibers with a microporous structure and strong and slidable double interfaces were fabricated by a continuous process involving wet-spinning, washing, crosslinking, and hot-pressing (Supplementary Fig. 1 and Supplementary Movie 1). $Ti_3C_2T_x$ MXene nanosheets were first obtained by etching the Al layer of the Ti_3AlC_2 MAX phase and exfoliating from accordion-like MXene. The as-prepared hydrophilic MXene nanosheets, with a lateral size and thickness of about 3 μm and 1.8 nm, respectively (Supplementary Fig. 2), formed a stable liquid crystal colloidal dispersion with polyrotaxane and PEDOT:PSS (Supplementary Fig. 3). This colloidal dispersion was continuously wet-spun into MXene fibers with long-range ordered nanosheet packing, microporous structure, and rugged fiber surfaces (Supplementary Fig. 4)[5,7]. After washing in DMSO to remove some PSS[26,27], the positively-charged semi-crystalline PEDOT engaged in electrostatic interactions with the negatively-charged MXene surface to form a strong MXene-PEDOT interface. After treatment in a crosslinking bath, the movable α-cyclodextrin (α-CD) units on the polyethylene glycol (PEG) chain of the polyrotaxane (Supplementary Fig. 5) were covalently crosslinked with the Ti−OH groups of MXene to produce a slidable MXene-polyrotaxane interface. The optimal initial weight ratio of MXene/PEDOT:PSS/polyrotaxane in the colloidal dispersion used for MXene fiber fabrication was 100:7:20 (Supplementary Fig. 6). The wet-spun MXene fiber with double interfaces was passed through a hot-press machine (optimized at 0.2 kPa and 70 °C, as discussed below) to regulate its porosity. Finally, the as-prepared MXene fibers were wet-coated with a layer of highly conductive and adherent AgNWs to further increase their electrical conductivity (Supplementary Fig. 7). Five types of MXene fibers were fabricated using the same wet-spinning and hot-pressing conditions for a comparison: pure MXene fibers without interfacial modification, MXene/PEDOT:PSS (PeM) fibers with strong interfaces, MXene/polyrotaxane (PrM) fibers with slidable interfaces, MXene/PEDOT:PSS/polyrotaxane (PPM) fibers with both strong and slidable interfaces, and PPM fibers coated with a AgNW network (A-PPM). All the MXene-based fibers exhibit high degree of nanosheet alignment after hot-pressing process (Supplementary Figs. 8–10).

Double-interfaces and microporous structure

The microporous structure within the MXene fibers was reconstructed using nanoscale X-ray computed tomography (Supplementary Fig. 11). Similar to deer antlers, which are composed of many internal canals and lacunae of various shapes and sizes, our PPM fiber had a high volume of spherical and tubular micropores. Cross-sectional scanning electron microscopy (SEM) images showed that the as-prepared PPM fibers exhibited similar microporous and lamellar structures to the compact bone of antler (Fig. 1c, d). Moreover, the porosity of PPM fibers decreased from 28.5 ± 3.2% to 7.7 ± 1.9% as the hot-pressing pressure increased from 0 kPa to 8 kPa (Fig. 1e). The SEM images clearly demonstrated that the compactness of the lamellar structure increased and the fiber surface became smoother as the applied hot-pressing pressure increased (Supplementary Fig. 12). Thus, hot pressing can be used to regulate the porosity, compactness, and morphology of MXene fibers.

Fourier-transform infrared (FT-IR) spectroscopy and X-ray photoelectron spectroscopy (XPS) were performed to confirm the formation of an MXene-polyrotaxane interface in the PPM fibers. Compared with pure MXene fibers, two new peaks appeared in both PrM and PPM fibers at 1743 cm^{-1} and 803 cm^{-1}, respectively, which were associated with ester stretching and Ti-O-C bonds (Fig. 1f)[5,28,29]. In addition, the XPS spectrum of the PPM fiber exhibited a new peak at 456.6 eV, which was attributed to Ti-O-C bonds (Fig. 1g)[5,28]. These findings indicate the successful crosslinking of the hydroxyl groups of the α-CD unit of the polyrotaxane with the Ti−OH groups of MXene via esterification, which led to the formation of a mechanically-interlocked MXene-polyrotaxane interface[5,28].

The formation of the MXene-PEDOT interface was also confirmed by FT-IR and XPS spectroscopy. After washing with DMSO to partially remove PSS (Supplementary Fig. 13), the C-S bond peak of PEDOT shifted from 716.5 cm^{-1} to 712.0 cm^{-1}, and the Ti−OH stretching band of MXene shifted from 3437.6 cm^{-1} to 3426.6 cm^{-1} in PPM fibers (Fig. 1h). These shifts indicated that the Ti-OH groups on the MXene sheets occupied the positions vacated by PSS, where they engaged in strong electrostatic coupling with the C-S bonds of PEDOT[30,31]. Moreover, the C 1 s XPS spectra revealed that after DMSO washing, the C-S and C-Ti-T_x groups of the PPM fibers shifted to a lower binding energy by 0.31 eV and 0.29 eV, respectively (Fig. 1i). These results verified the formation of electrostatic interactions between Ti-OH groups on MXene and C−S bonds in PEDOT[32,33]. To elucidate the strong interfacial interactions between MXene and PEDOT, we conducted density functional theory (DFT) calculations and electron localization function (ELF) analysis (Supplementary Fig. 14). The calculated binding energy of MXene-PEDOT (−2.66 eV) was stronger than that of the MXene-MXene interface (−1.88 eV). Minimal localized electrons were present between the MXene-MXene interface, while substantial localization was observed between the MXene-PEDOT interface. To further differentiate interfacial interactions between PEDOT and MXene, the reduced density gradient (RDG) was plotted in Fig. 1j to facilitate energy scaling via noncovalent interaction (NCI) index analysis[34]. The more negative (λ2)ρ values (−0.031) indicate a greater electron density, suggesting that PEDOT impeded interlayer slip at the atomic scale, indicating stronger PEDOT-MXene interactions[34]. These analyses verify that the

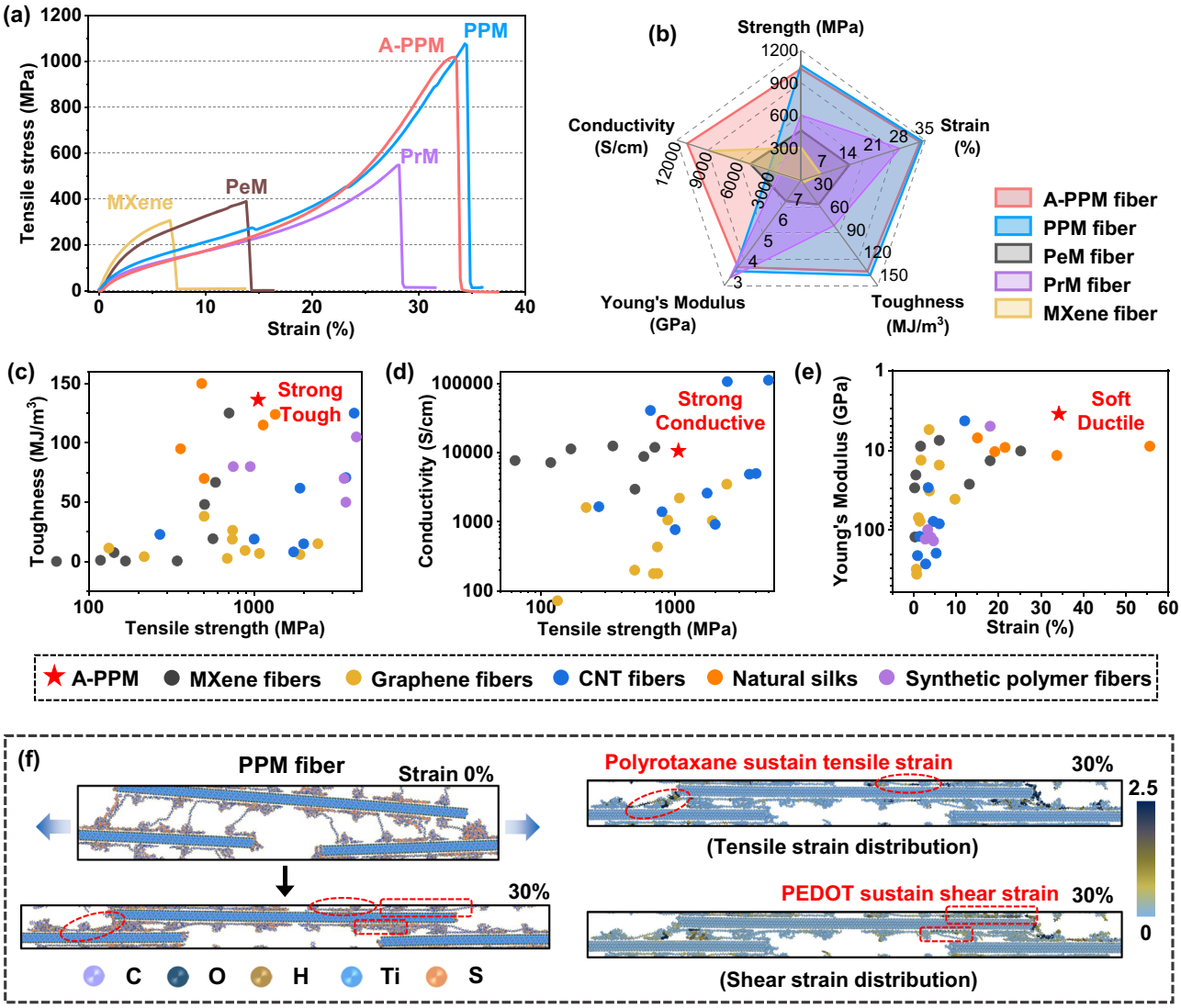

Fig. 2 | Mechanical properties of MXene/PEDOT:PSS/polyrotaxane (PPM) fiber regulated by double-interfaces. a Typical stress-strain curves of MXene, MXene/PEDOT:PSS (PeM), MXene/polyrotaxane (PrM), PPM, and PPM fibers coated with a AgNW network (A-PPM). **b** Radar maps of the mechanical and electrical properties of MXene, PeM, PrM, PPM, and A-PPM fibers. Ashby diagrams of (**c**) toughness versus tensile strength (**d**) electrical conductivity versus tensile strength and (**e**) Young's Modulus versus strain of A-PPM fibers and other conventional fibers. The data used are summarized in Supplementary Table 1. **f** MD simulation snapshots and strain distribution of PPM fibers. Red dashed circles highlight the molecular motions responsible for bearing concentrated strain.

electrostatic interactions in MXene-PEDOT were much stronger than the hydrogen bonds formed between the MXene-MXene interface.

Mechanical properties

Figure 2a and Supplementary Fig. 15 show the monotonic tensile stress-strain curves for all types of MXene fibers. As a control sample, the pure MXene fibers showed an average ultimate strength, failure strain, toughness, Young's Modulus, and electrical conductivity of 302.1 ± 8.3 MPa, 6.3 ± 0.3%, 13.2 ± 1.3 MJ m^{-3}, 8.2 ± 0.3 GPa, and 8807.7 ± 102.3 S cm^{-1}, respectively, which were consistent with those of typical oriented MXene fibers[4,6,7,11]. In comparison, the PeM fibers with a strong MXene-PEDOT interface demonstrated a higher strength, ductility, and toughness of 406.4 ± 31.8 MPa, 14.2 ± 0.8%, and 37.9 ± 2.9 MJ m^{-3}, respectively. This indicates that the introduction of strong interfaces into the lamellar structure of MXene fibers enhanced their mechanical properties[35]. The ultimate strength, failure strain, and toughness of PrM fibers with a slidable MXene-polyrotaxane interface further increased to 596.8 ± 13.2 MPa, 27.9 ± 0.7%, and 70.4 ± 3.7 MJ m^{-3}, respectively. This confirms that the polyrotaxane chains served as molecular-scale bridges between MXene nanosheets to improve the interfacial interactions, which strengthened the fibers. The sliding of the mechanically-interlocked network dissipated large amounts of energy, which toughened the fibers[5]. Moreover, although both PrM and PeM exhibit high orientation factors, the polyrotaxane's pulley effect under mechanical load further facilitates the sliding and alignment of MXene nanosheets, leading to an additional increase in orientation[5]. This synergistic mechanism allows PrM to achieve superior tensile strength and toughness despite only a marginal difference in orientation. Notably, the PPM fibers with a synergy of strong and slidable interfaces and optimized fiber diameter (diameter about 50 μm, Supplementary Fig. 16) achieved record-high tensile strength, failure strain, and toughness of 1060.1 ± 33.5 MPa, 34.2 ± 1.8%, and 136.1 ± 6.5 MJ m^{-3}, respectively (Fig. 2b)[36]. Despite its high strength, the PPM fibers were soft, with a Young's modulus (3.5 ± 0.4 GPa) much lower than that of MXene fibers and well within the typical range for fibers used to create comfortable textiles[37]. The slidable interface and

microporous structure played a vital role in reducing the stiffness and increasing the softness of the PPM fibers[28,29].

After coating with the AgNW network, the A-PPM fibers demonstrated an electrical conductivity of 10575.3 ± 312.3 S cm^{-1}, which was approximately 3.5 times higher than that of PPM fibers (3105.3 ± 68.2 S cm^{-1}) (Supplementary Fig. 15 and Fig. 2b). This significant increase of electrical conductivity on A-PPM fiber is mainly attributed to the intrinsically high conductivity of AgNWs (~6.3×10^5 S cm^{-1}) coated on the fiber surface[38,39]. The AgNW content was controlled at around 6.9 wt% during the coating process. Importantly, the A-PPM fibers maintained the same stress-strain response and mechanical properties as PPM fibers, with negligible deterioration (Fig. 2a). The resulting A-PPM fibers exhibited a specific strength of 361 ± 9 MPa/(g cm^{-3}) and a specific electrical conductivity of 364.8 ± 8 S·m^2 kg^{-1} with a density of about 2.88 g cm^{-3}. Additionally, A-PPM fibers demonstrated high stability in mechanical properties and electrical conductivity across different samples and batches (Supplementary Fig. 17). Overall, the A-PPM fiber showed seemly paradoxical but exceptional tensile strength and toughness that surpassed the values of all reported MXene fibers and were also comparable to the highest values of natural silks (Fig. 2c)[17,18,40,41]. Compared with most carbon nanotubes (CNTs) and graphene fibers with gigapascal strength, our A-PPM fibers achieve superior conductivity and toughness (Fig. 2d)[14,15,42,43]. In addition, while Toray and Dyneema carbon fibers exhibit superior tensile strength (>3 GPa) and modulus (>100 GPa), our A-PPM fibers demonstrate unique advantages for electronic textiles, combining high conductivity (>10^4 S cm^{-1}) with exceptional toughness (>130 MJ m^{-3}) and remarkable ductility (breaking elongation >30% versus <6% for Toray and Dyneema carbon fibers) (Supplementary Table 1). Moreover, the softness and ductility of A-PPM fibers greatly exceeded those of all previously reported MXene, graphene, and CNT fibers. It even surpassed those of some natural and synthetic polymer fibers for textiles (Fig. 2e)[38,44,45]. Thus, our A-PPM fiber exhibited a rare combination of ultrahigh strength, toughness, and electrical conductivity while also maintaining a high softness and ductility, which have never been obtained by any natural or synthetic fiber materials (Supplementary Table 1).

Double-interface effect

To elucidate the effects of MXene-PEDOT and MXene-polyrotaxane interfaces on the MXene fibers' mechanical properties, we performed large-scale molecular dynamics (MD) simulations for PeM, PrM, and PPM fibers under uniaxial tension (Fig. 2f and Supplementary Note 3). Representative snapshots and atomic strain distributions were plotted to provide molecular-level insights into the deformation mechanisms (Supplementary Figs. 18–21). Because the MXene fibers exhibited typical characteristics of staggered nanosheets, load transfer between adjacent MXene nanosheets occurred via the shearing of intercalated polymers[46,47]. In PeM fibers with an MXene-PEDOT interface, PEDOT created physical crosslinks that could only sustain interfacial shear deformation. This led to a low interfacial strength and limited load transfer between MXene interlayers (Supplementary Fig. 18, and Supplementary Movie 2). In PrM fibers with MXene-polyrotaxane interfaces, the atomic strain distributions showed that PEG chains bore the tensile strain, while the shear strain was mainly concentrated at the fixed α-CD rings. This prevented effective interlayer load transfer (manifested as localized deformation) of PrM fibers under a large tensile strain (Supplementary Fig. 19, and Supplementary Movie 2). As for the PPM fibers, the double interfaces cooperated well with each other during the tensile process (Fig. 2f, Supplementary Fig. 20, and Supplementary Movie 2). When stretched to 30% strain, the polyrotaxane chains mainly bore the tensile strain, while the PEDOT domains bore the interfacial shear stress, thus maintaining load transfer between adjacent MXene nanosheets. Therefore, the existence of the MXene-PEDOT interface delayed strain localization to the MXene-polyrotaxane interface, allowing the PPM fibers to utilize abundant polyrotaxane chains more effectively before fracturing. These synergistic effects simultaneously increased the extensibility, strength, and toughness of PPM fibers. MD simulation results show good overall agreement with the experimental data in terms of qualitative trends (Supplementary Fig. 21 and Supplementary Table 2), with both datasets consistently identifying PPM fibers as exhibiting superior mechanical properties, including strength, extensibility, and toughness, among the three fiber samples studied.

Micropore effect

Next, we investigated how the microporous structure affected the mechanical properties of the PPM fiber. As internal voids are considered to be the dominant factor deteriorating the mechanical properties of lamellar fibers[4,8,15], densification strategies have been widely used to enhance the tensile strength of MXene fibers[4,8,14,15]. PeM fibers with only a strong interface also exhibited a higher tensile strength as the porosity decreased (Fig. 3a and Supplementary Fig. 22), but changes in the mechanical performance of PPM fibers upon decreasing their porosity showed a different trend (Fig. 3b and Supplementary Fig. 23). The tensile strength, extensibility, and toughness of PPM fibers before hot-pressing were lower due to their high porosity (28.5%). Notably, these mechanical properties increased to their highest values when the porosity decreased to 20.8% after hot-pressing at 0.2 kPa, followed by a progressive decrease as the porosity further decreased to 11.8% (Fig. 3c). These results suggest that the microporous structure played a different role in the PPM fiber with distinct strong and slidable double interfaces. The high volume of micropores greatly decreased the stiffness and increased the softness of the PPM fiber, making it even softer than polymer fibers[48]. Since the slidable interface facilitated the sliding of MXene nanosheets[5,29], the micropores may have dissipated energy and provided more room for a higher degree of sliding and alignment of MXene nanosheets in the lamellar fibers. This alleviated internal strain/stress concentration (Fig. 3d)[49]. Comparative SEM analysis at 0%, 20%, and 30% strain clearly demonstrates progressive pore deformation (Supplementary Figs. 24 and 25), with the elliptical pores becoming increasingly compressed along the tensile axis. This morphological evolution directly creates additional space for chain sliding at interfaces.

A numerical model based on the finite element method (FEM) was adopted to investigate the stress distribution and fracture mechanism in the lamellar and porous MXene fibers with slidable (Fig. 3e and Supplementary Fig. 26a) and non-slidable interfaces (Fig. 3f and Supplementary Fig. 26b) under a uniaxial tensile load (Supplementary Note 4). The entire model consisted of a brick-mud-like structure with a small elliptical hole. As the load increased, the slidable interface model reached the initial criterion of failure, resulting in interface sliding. This released stress concentrated at the interface and significantly reduced the stress within the structure. Local stress concentration occurred at the small hole during stretching, causing the interface to first slide around the hole, which was followed by outward stress release. The hole provided room for a long slip distance at the slidable interface, thus allowing the lamellar structure to maintain its load-bearing capacity over a large deformation range. In contrast, it was difficult for the non-slidable interface model to reach its failure criterion, thereby maintaining a high stress concentration within the structure, especially around the hole. The non-slidable interface quickly led to structural failure once failure was initiated at the small hole.

Mechanical elasticity and durability

Textile fibers are usually subjected to repeated bending and stretching during wear. Elasticity and durability are highly desired but difficult to realize in conventional MXene fibers[50,51]. The results showed that both

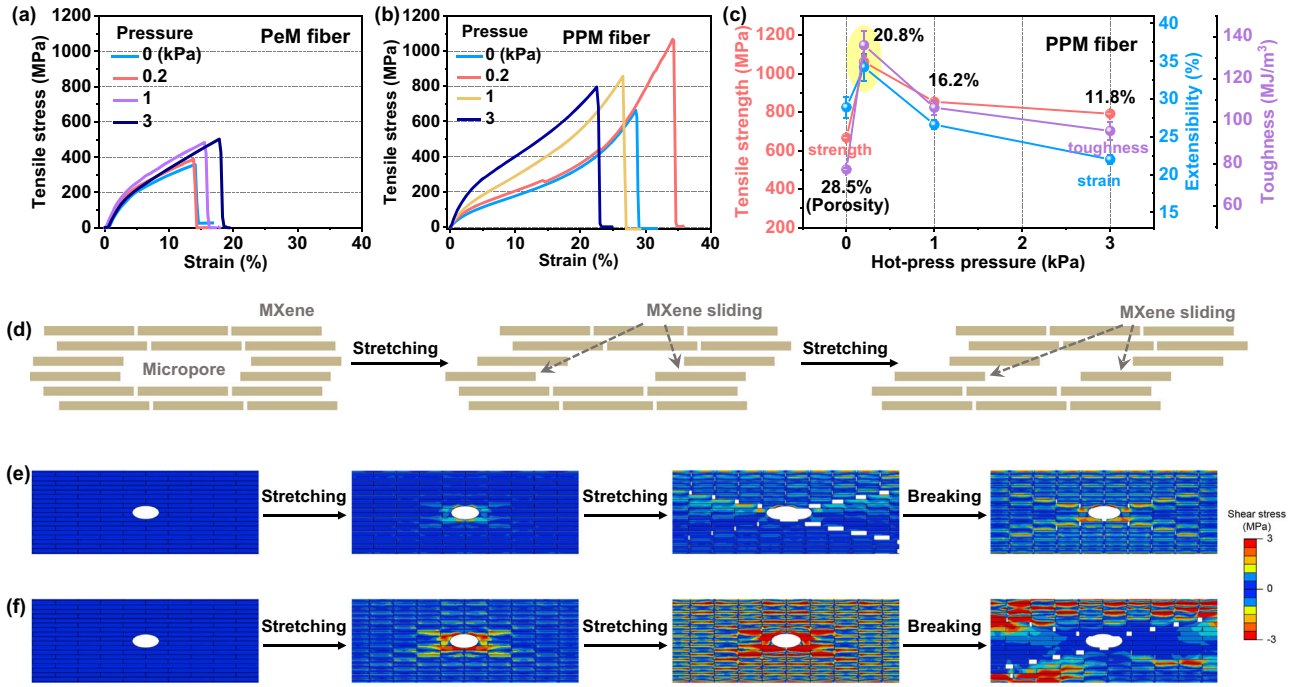

Fig. 3 | Regulation of mechanical properties of MXene/PEDOT:PSS/polyrotaxane (PPM) fibers by micropores. Representative stress-strain curves of (**a**) MXene/PEDOT:PSS (PeM) and (**b**) PPM fibers fabricated under hot-pressing pressures of 0 kPa, 0.2 kPa, 1 kPa, and 3 kPa, respectively. **c** Comparison of the tensile strength, toughness, and ductility of PPM fibers with porosities of 28.5%, 20.8%, 16.2%, and 11.8%. The error bars represent the mean ± standard deviation (n = 5 independent experiments). **d** Proposed mechanism wherein the micropores provided room for MXene sliding in PPM fibers. FEM simulations of stress distribution in lamellar and porous MXene fiber with (**e**) a slidable interface and (**f**) a non-slidable interface when subjected to a uniaxial tensile load.

PPM and A-PPM fibers did not display an apparent yield point or well-defined plastic flow region in their stress-strain curves (Fig. 2a), indicating their rubber-like properties[52]. We measured the cyclic loading-unloading tensile curves of a stretched A-PPM fiber (under 20% strain) by increasing its strain from 23% to 26% (Fig. 4a) and also by cyclic tensile tests between strains of 0–3%, 10–13%, 15–19%, and 20–26% (Fig. 4b and Supplementary Fig. 27). The A-PPM fibers showed a high elastic recovery with negligible residual strain during their stretch-release cycles (Fig. 4c and Supplementary Movie 3). This exceptional elasticity, which has rarely been observed in inorganic-matrixed function fibers, may stem from the strong interfaces, which functioned as crosslink points to stabilize the permanent form of the fiber, while the slidable interfaces acted as switches that triggered the recovery of deformed fibers[36,53]. Due to their rubber-like deformability, A-PPM fibers showed excellent durability and fatigue resistance. The electrical resistance of the A-PPM fibers slightly increased by 6.2% when stretched to 25% strain (Fig. 4d), and their current-carrying capacities remained almost constant, even when stretched to 30% strain (Fig. 4e). The AgNWs on A-PPM fibers can retain relatively intact network structure with better alignment along the strain direction when stretched to 25% strain (Supplementary Fig. 28). Moreover, unlike conventional conductive fibers that easily lose their electrical conductivity after repeated bending or stretching, our A-PPM fibers exhibited a slight conductivity increase after more than 100000 stretch-release cycles between 20% and 26% strain (Fig. 4f). This increase in conductivity may be due to the better alignment of AgNWs along the axis direction during the stretching cycles.

A-PPM also exhibits excellent environmental and long-term stability. Thermomechanical characterization of A-PPM fibers via Dynamic Mechanical Analysis (DMA) demonstrated good modulus stability (−30 °C to 120 °C) under cyclic tensile loading (Supplementary Fig. 29). The invariant mechanical response confirms exceptional thermal durability, making these fibers suitable for applications requiring performance across extreme temperature variations. Moreover, The A-PPM fibers demonstrated excellent humidity stability, maintaining <2% conductivity variation across 33-85% relative humidity (RH) environments (Supplementary Fig. 30b) and retaining >96% conductance after storage for 30 days under RH of 85% and environmental temperature of 20 °C (Supplementary Fig. 31). Mechanical characterization revealed consistent tensile strength, toughness and stress-strain behavior under varying humidity (Supplementary Fig. 30a), confirming robust resistance to both moisture and oxygen degradation. The A-PPM fibers also demonstrated exceptional UV stability, maintaining >98% conductivity and unchanged mechanical properties after 180 mins of 300 W UV exposure (Supplementary Fig. 32). Specifically, the microporous structure and the dual-crosslinked interface work synergistically to endow the fibers with excellent strength, toughness, and structural stability. Furthermore, they effectively prevent the penetration of moisture and oxygen, thereby maintaining structural integrity under harsh environmental conditions. Notably, the A-PPM fiber maintains excellent mechanical properties even after 7 and 14 days of storage, with stress levels consistently around 1 GPa without significant degradation. After 14 days of storage, the fiber still demonstrates high electrical conductivity of 10284 ± 324.9 S cm^{-1}, further confirming its excellent stability (Supplementary Figs. 33 and 34).

We further evaluated the potential for medical implantation and biocompatibility of the fibers through cytotoxicity experiments. Human Skin Fibroblasts (HSF) cells are cultured with the leaching solution of the fibers for a certain period to assess the cytotoxicity of the fibers. Compared to the untreated control group, neither fibers-treated group showed a significant reduction in cell number, with cell viability remaining consistently high at 98.4% (1 μg mL^{-1}) and 98.8% (10 μg mL^{-1}) after incubation, demonstrating excellent biocompatibility and only slight concentration-dependent variations. (Supplementary Figs. 35 and 36). These findings indicate that the MXene-based

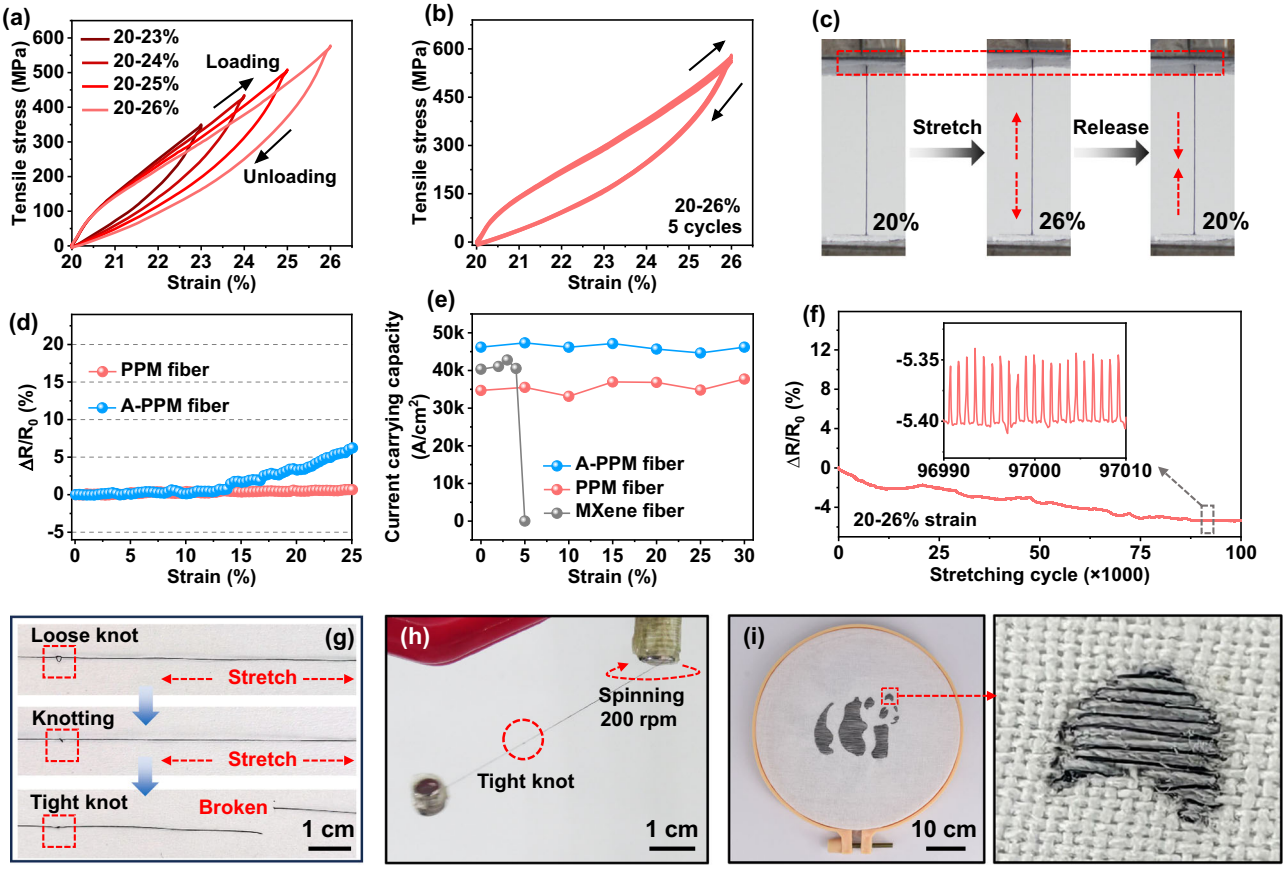

Fig. 4 | Elasticity and durability of PPM and A-PPM fibers. a Loading-unloading tensile curves of stretched A-PPM fiber at an initial 20% strain and upon stretching to 23-26% strain. **b** Five loading-unloading cycles of A-PPM fiber between 20% and 26% tensile strain. **c** Photographs of a 3-cm-long A-PPM fiber stretched from 20% to 26% strain and then recovered to 20% strain. **d** Relative resistance changes as a function of tensile strain for PPM and A-PPM fibers. **e** Changes in the current carrying capacity as a function of tensile strain for pure MXene, PPM, and A-PPM fibers. **f** Relative resistance changes of an A-PPM fiber over 100000 stretch-release cycles between 20% and 26% strain. **g** Photographs of a tied A-PPM fiber stretched to form a tight knot, which broke at a point far from the knot. The red rectangle highlights the position of the knot. **h** Photograph of a tied 6-cm-long A-PPM fiber with a tight knot lifting a load more than 12,000 times greater than its own weight and spinning at 200 rpm. The red circle highlights the position of the knot. (**i**) Photograph of an embroidered panda made of A-PPM fibers and cotton fibers.

fibers exhibit negligible cytotoxic effects on HSF cells, further supporting their favorable biocompatibility.

We also investigated the knottability and weavability of our MXene fibers, as these properties are essential for textile processes. The combination of high softness and elasticity allowed the A-PPM fibers to be folded and tightly knotted without breaking or cracking (Supplementary Fig. 38). The high modulus and limited ductility of conventional MXene and carbon-based fibers led to defect formation in their knot points, resulting in fiber fracture at knots[14,54–56]. In contrast, the knotted A-PPM fibers exhibited different mechanical behavior, and they fractured far from the knot (Fig. 4g and Supplementary Movie 4). We demonstrated that a knotted A-PPM fiber sample could lift a load more than 12000 times heavier than its own weight and spin at 200 rpm without breaking (Fig. 4h and Supplementary Movie 5), indicating a high knotting efficiency[54]. Moreover, due to their high mechanical strength and toughness, the A-PPM fiber could be woven or embroidered into intricate patterns on cotton textiles (Fig. 4i and Supplementary Fig. 39). After wet-coating with a hydrophobic polydimethylsiloxane layer, the encapsulated A-PPM fiber exhibited excellent waterproofness and washability, with its electrical conductivity remaining unchanged after 50 washing and drying cycles (Supplementary Fig. 40). These results indicate that our A-PPM fibers have good elasticity, durability, weavability, and washability, making them suitable for practical textile applications.

Electronic fiber applications

Their excellent mechanical and electrical properties make the MXene fibers an ideal candidate for use with electronic fibers. As a proof of concept, we developed two types of sensory fibers from A-PPM fibers to demonstrate their application feasibility in smart textiles. First, with their high strength, ductility, and toughness, we twisted three A-PPM fibers into a single fiber bundle electrode (Supplementary Fig. 41), followed by coating a thin layer of polyurethane as a dielectric (Fig. 5a, b). Two bundle electrodes were then twisted together to form a pressure-sensitive fiber sensor (Pressure-FS) that could detect pressure through capacitance changes induced by a change in the contact area with polyurethane (Fig. 5a, b). The internal microporous structure, in conjunction with the wrinkled fiber surface, enhanced its capacitive response under force stimuli[57,58]. Additionally, the wrinkled fiber surface morphology enhances effective interfacial contact area and promotes mechanical interlocking with the dielectric layer, thus stabilizing capacitance under mechanical stress. The resultant Pressure-FS exhibited stable capacitance changes under cyclic transient force (Fig. 5c and Supplementary Fig. 42a), a rapid response and recovery of less than 57 ms (Supplementary Fig. 42b), and a durable capacitive response for more than 1000 loading-unloading cycles (Fig. 5d). The excellent linearity (R^2 = 0.998 for 0-0.003 N and 0.982 for 0.003-0.01 N) ensures reliable measurements (Supplementary Fig. 43), while the fast response time and high precision (0.001 N detection

https://doi.org/10.1038/s41467-025-64647-w

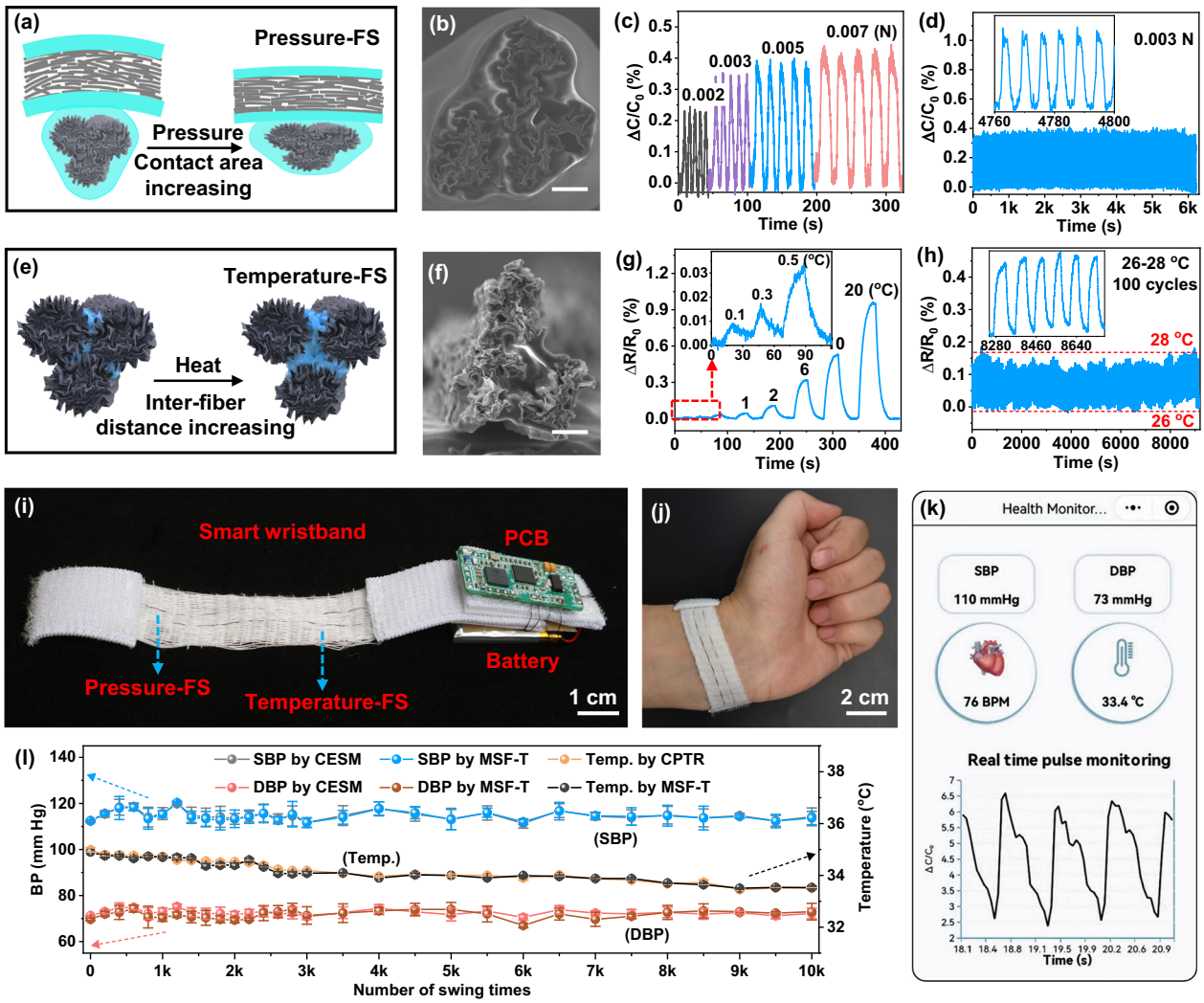

Fig. 5 | Sensory fibers, smart textiles, and health-monitoring applications. **a** Schematic showing the structure and sensing mechanism of pressure-sensitive fiber sensor (Pressure-FS) based on A-PPM fibers. **b** Cross-sectional SEM image of Pressure-FS (repeated independently with similar structures for 5 times). Scale bar is 30 μm. **c** Relative capacitance changes over time of Pressure-FS by varying the force in the range of 0.002–0.007 N. **d** Relative capacitance changes of a Pressure-FS for 1000 pressure loading-unloading cycles under a load of 0.003 N. Inset: Detailed capacitance change curves recorded between 4760 s and 4800 s. **e** Schematic showing the structure and sensing mechanism of temperature-sensitive fiber sensor (Temperature-FS) based on A-PPM fibers. **f** Cross-sectional SEM image of Temperature-FS (repeated independently with similar structures for 5 times). The scale bar is 30 μm. **g** Relative resistance changes over time of Temperature-FS at temperatures from 0.1 °C to 20 °C. **h** Relative resistance changes of Temperature-FS for 100 heating and cooling cycles between 26 °C and 28 °C. **i** Photograph of an integrated smart wristband composed of a Pressure-FS, a Temperature-FS, a signal-processing circuit, and a battery. Photographs of (**j**) a smart wristband worn on a human wrist for (**k**) the real-time monitoring of physiological signals, including arterial pulse waveforms, blood pressure, and skin temperature, transmitted and displayed in a customized smartphone application. **l** Blood pressure and skin temperature signals measured by a smart wristband worn on a volunteer's wrist for 10000 cycles of swinging a badminton racket. The signals were also measured by a medical-grade commercial cuff-based electronic sphygmomanometer (CESM) and paperless temperature recorder (CPTR). The error bars represent the mean ± standard deviation ($n = 4$ independent experiments).

limit) enable real-time monitoring of subtle pressure changes (Supplementary Fig. 44 and Table 4).

We also fabricated a temperature-sensitive fiber sensor (Temperature-FS) capable of monitoring temperature changes through resistance changes. The sensory fiber was assembled by twisting three A-PPM fibers into a single fiber bundle, which was then dip-coated in a polyethylene oxide (PEO) aqueous solution (Fig. 5e). After drying, a semi-crystalline PEO layer covered the microgrooves of the fiber bundle and filled the gaps between A-PPM fibers (Fig. 5f and Supplementary Fig. 45). This semi-crystalline PEO underwent a crystalline-to-amorphous transition with a large volume expansion near its melting point (Supplementary Fig. 46), which increased the inter-fiber distance and, thus, the resistance of the fiber bundle[59,60]. Moreover, the multi-level surface structure of the A-PPM fibers not only provides additional contact points but also enhances the interfacial bonding between the fibers and PEO, ensuring the stability of the temperature-sensing fiber over multiple thermal cycles. The resultant Temperature-FS demonstrated a temperature-sensing accuracy of 0.1 °C (Fig. 5g), rapid sensing (Supplementary Figs. 47 and 48b), and stable sensing for many heating-cooling cycles (Fig. 5h). Specifically, the sensor demonstrated precise detection capability across a broad temperature range (25–45 °C) while maintaining exceptional linearity ($R^2 = 0.996$) in its temperature response (Supplementary Fig. 48a and Table 5).

The sensors exhibit excellent environmental stability and long-term reliability. The Pressure-FS maintains highly stable capacitive responses to 0.005 N and 0.007 N stimuli across a broad humidity

range (33-85% RH), demonstrating excellent humidity resistance (Supplementary Fig. 49). Similarly, the Temperature-FS shows consistent performance under varying humidity conditions (Supplementary Fig. 50). Beyond humidity resilience, both sensors retain precise temperature/pressure detection accuracy even after 200 bending cycles, highlighting their mechanical durability and interference resistance (Supplementary Figs. 51 and 52). Long-term stability tests further confirm their robustness. After 7 and 14 days of storage, the sensors preserve nearly identical response curves with minimal deviation in linearity (Supplementary Figs. 53 and 54). Additionally, batch consistency assessments demonstrate high reproducibility across production batches and individual specimens, confirming manufacturing robustness (Supplementary Figs. 55 and 56). These superior properties, combined with the fiber's high strength, toughness, and softness, enable it to withstand complex processing while delivering exceptional performance in wearable sensing applications.

In addition to working as single fiber devices, the sensory fibers could also be woven into textiles for smart textile applications. We integrated a smart wristband with a Pressure-FS, a Temperature-FS, commercial Nylon fibers, a printed circuit board (PCB, with a built-in Bluetooth module, Supplementary Fig. 57), a battery, and a customized smartphone application (Fig. 5i and Supplementary Fig. 58). The smart wristband closely adhered to a human wrist to collect multiple high-fidelity physiological signals, including arterial pulse waveforms and body temperature (Fig. 5j and Supplementary Fig. 59). The smart wristband exhibits excellent signal selectivity, with its pressure sensors maintaining stable sensitivity within the 20–40 °C range while showing negligible pressure-response variations, and its temperature sensors demonstrating consistent accuracy under varying applied pressures. This performance confirms each sensor's high specificity to its designated stimulus with minimal cross-sensitivity between parameters(Supplementary Figs. 60–62).The measured pulse wave signals were transmitted to the smartphone application in real-time and processed by a custom program to obtain the systolic blood pressure (SBP) and diastolic blood pressure (DBP) (Fig. 5k, Supplementary Fig. 63, Supplementary Note 6, 7). A medical-grade commercial cuff-based electronic sphygmomanometer (CESM) and paperless temperature recorder (CPTR) were used as references to assess the accuracy and reliability of our smart wristband (Supplementary Figs. 64–66). In a Bland-Altman analysis from 30 participants, the absolute mean error (m.e.) and standard deviation of the error (s.d.) between the smart wristband and CESM was 0.377 ± 4.159 mmHg for SBP and 0.445 ± 2.428 mmHg for DBP, respectively (Supplementary Fig. 65, Supplementary Note 8), indicating the highest grade of accuracy for the smart wristband as per the IEEE standard[61,62]. In addition, the smart wristband achieves rapid blood pressure measurement within 3.5 seconds and this allows for the detection of transient blood pressure fluctuations (e.g., in neurogenic disorders or stress responses). This capability supports rapid alerts in high-risk environments (e.g., workplace heat stress) and complements existing static diagnostic technologies.

A volunteer was asked to perform various exercises while wearing a smart wristband to non-invasively monitor his real-time physiological status (Supplementary Movies 6–10). The measured physiological data remained stable and showed strong resistance against external interference, including environmental changes and hand movements (Supplementary Fig. 67). Figure 5l shows a volunteer wearing the smart wristband and swinging a badminton racket more than 10000 times. Each swing cycle involved the motions of gripping, clearing, and smashing a racket, which led to continuous and large deformation of the A-PPM fibers within the wristband (Supplementary Fig. 68). Notably, the SBP, DBP, and skin temperature data obtained by the smart wristband were highly consistent with those measured by commercial sensors during this almost 8-hour-long vigorous exercise (Fig. 5l). This demonstrates the robustness, reliability, and durability of the smart wristband for practical applications.

Discussion

We have overcome the long-standing mechanical issues to assemble functional MXene fibers. In direct contrast to general strengthening approaches for conventional structural materials (i.e., the removal of pores and increasing compactness), we instead proposed an deer antler-inspired strengthening and toughening strategy. In this strategy, strong and slidable double interfaces were constructed to cooperate with internal micropores in lamellar MXene fibers. We introduced semi-crystalline PEDOT to form a strong interface with MXene to bear shear stress and crosslinked polyrotaxane with MXene nanosheets to form a slidable interface to bear tensile strain. The slidable interface could also cooperate with the micropores to alleviate internal stress concentration. Using this biomimetic design, our PPM fibers exhibited a substantial increase in their overall load-bearing and energy-dissipating capacity, achieving record-high tensile strength (>1 GPa), ductility (>30% strain), and toughness (>130 MJ m^{-3}). After coating with a conductive AgNW network on the surface, the resultant A-PPM fibers exhibited an electrical conductivity of over 10500 S/cm. Notably, this MXene-matrix fiber exhibited elasticity and endured over 100000 stretching cycles without a degradation in its electrical conductivity, and was also as soft as polymer fibers. Due to these exceptional mechanical and electrical properties, a smart wristband made of our biomimetic fiber realized reliable, robust, real-time, and non-invasive monitoring of human physiological signals. This deer antler-inspired strategy may bring functional fibers one step closer to broader applications.

There remain certain limitations for the large-scale application of these fibers. The synthesis and purification processes of polyrotaxanes and AgNWs still rely on organic solvents, raising concerns regarding environmental impact and scalability. Additionally, the carbon emission factors during production may increase accordingly. To address these challenges, future work should focus on developing greener alternatives, including improved aqueous systems and closed-loop recycling, along with utilizing renewable energy and further simplifying the preparation process.

Methods

Raw materials

Ti_3AlC_2 powders (particle size ~400 mesh) were obtained from Laizhou Kai Kai Ceramic Materials Co., Ltd.). PEDOT:PSS aqueous solution (Clevios PH 1000) was purchased from Anhui Zesheng Technology Co., Ltd. (Anhui, China). (2-Hydroxypropyl)-α-cyclodextrin (HP-α-CD) was purchased from Sigma-Aldrich. Amino-terminated PEG (PEG-NH_2, $Mw = 20{,}000$) and PEO were purchased from Shanghai Yuanye Biotechnology Co., Ltd. (Shanghai, China). N-α-Carbobenzoxy-L-glutaminyl-glycine (Z-Gln-Gly) was purchased from Shanghai Bide Pharmaceutical Technology Co., Ltd. (Shanghai, China). Glutamine transaminases (TGases) were purchased from Beijing Soleibo Technology Co., Ltd. (Beijing, China). Methanol was purchased from Tianjin Kangkede Technology Co., Ltd. (Tianjin, China). N, N′-carbonyldiimidazole (CDI) was purchased from Tianjin Xiensi Aopude Technology Co., Ltd. Acetic acid was purchased from Acros Organics. Dimethyl sulfoxide (DMSO), tetrahydrofuran (THF) and lithium fluoride (LiF) were purchased from Aladdin Reagent. AgNWs were synthesized based on our previously reported method, with an average diameter of 40 nm and a length of 20 μm[63,64].

Synthesis of $Ti_3C_2T_x$ MXene nanosheets

The dispersions of MXene nanosheets were prepared as follows. 2 g of LiF was dissolved in 40 mL HCl solution (9 M) and stirred for 30 min. Subsequently, 2 g Ti_3AlC_2 powder (400 mesh) was slowly added and continually stirred at 35 °C for 24 h. After completely reacting, the resulting mixture was washed by repeated centrifugation at 685 × g for 10 min until the pH of the supernatant was greater than 5. The precipitated MXene layer at the bottom was dispersed in ethanol using

ultrasonication for 30 min. Subsequently, the dispersion was centrifuged at 5590 × g for 30 min. In the next step, after adding distilled water, the precipitate was sonicated for 20 min and then centrifuged at 685 × g to form a uniform MXene suspension. Finally, the resulting homogeneous MXene solution was freeze-dried to obtain MXene powder.

Synthesis of polyrotaxane

Polyrotaxane was synthesized by employing a one-pot method, as illustrated in Supplementary Fig. 5. Initially, a solution was prepared by dissolving 1 g of HP-α-CD in 3 mL of PBS (0.1 mol L^{-1}, pH 8.0). Subsequently, 0.2 g of PEG-NH_2 was added to the solution and stirred for 1 h until achieving a clear solution. The resultant mixture was then refrigerated at 4 °C for 36 h. For the end-capping reaction, Z-Gln-Gly (0.08 g) and TGase (10 mg) were added to the mixture and stirred at room temperature for 3 days. Then, the above mixture was dialyzed (MWCO: 8000 − 14000 g mol^{-1}) to remove free Z-Gln-Gly, HP-α-CD, and TGase. After freeze-drying, the rough product was washed with THF to remove free PEG and then dialyzed again for 48 h. The dialyzed solution was filtered through a 0.45 μm membrane filter and then freeze-dried to obtain the final product.

Fabrication of pure MXene fiber

First, MXene nanosheets were dispersed in deionized water to form a low-concentration dispersion (5 mg mL^{-1}). Then, a high-concentration MXene dispersion (170 mg mL^{-1}) was obtained by concentrating the dispersion via centrifugation at a constant volume. The MXene spinning solution (1 mL) was added to a 3 mL syringe (Becton Dickinson), and a 90° curved blunt needle (26 G) was fixed onto the syringe. The spinning solution was extruded through a needle spinneret into a rotating coagulation bath at a velocity of 5 mL h^{-1} to form the initial fibers. The coagulation bath was a mixed solution containing acetic acid and DMSO in a volume ratio of 5:1. The resulting fibers were subsequently passed through a a hot-press machine at 70 °C. Finally, the fibers were collected and placed in a glove box for 12 h before use.

Fabrication of PeM fiber

The commercial PEDOT:PSS was concentrated and filtered before being added to the concentrated MXene dispersion (170 mg mL^{-1}). Then, the MXene/PEDOT:PSS dispersion was vortexed for 3 h at room temperature. Finally, the composite spinning solution was sonicated for 5 min, degassed, and stored for further use. The mass fractions of PEDOT:PSS in the composite spinning solution were 3, 7, and 11 wt%, respectively. The MXene/PEDOT:PSS spinning solution (1 mL) was added to a 3 mL syringe (Becton Dickinson), and a 90° curved blunt needle (26 G) was attached to the syringe. The coagulation bath and spinning conditions for PeM fiber were consistent with those employed for pure MXene fibers. The fibers were collected on reels and then soaked in a DMSO washing bath for 30 min at 60 °C, followed by soaking in a methanol solution for 20 min at room temperature. DMSO can facilitate the strong dissociation of PSS − H^+ chains into PSS anions and protons, thereby reducing its interaction strength with PEDOT and consequently enhancing its electrical conductivity. The resulting fibers were subsequently passed through a hot-press machine at 70 °C. Finally, the fibers were collected and placed in a glove box for 12 h before use.

Fabrication of PrM fiber

First, polyrotaxane was dissolved in a small amount of deionized water, and the obtained dispersion was added to the MXene dispersion (170 mg mL^{-1}) and vortexed for 3 h at room temperature. Finally, the composite spinning solution was sonicated for 5 min and degassed for further use. The mass ratios between MXene and polyrotaxane were 5:1, 4:1, and 3:1, respectively. The MXene/polyrotaxane spinning solution (1 mL) was added to a 3 mL syringe (Becton Dickinson), and a 90° curved blunt needle (26 G) was attached to the syringe. The coagulation bath and spinning conditions for PrM fiber were the same as those used for the pure MXene fibers. Finally, the fibers were collected on reels and soaked in a crosslinking bath (CDI/DMSO solution with 2.27 wt% CDI) for 30 min at 60 °C, followed by soaking in a methanol solution for 20 min at room temperature. The resulting fibers were subsequently passed through a a hot-press machine at 70 °C. Finally, the fibers were collected and placed in a glove box for 12 h before use.

Fabrication of PPM fiber

First, the polyrotaxane was dissolved in a small amount of deionized water. The polyrotaxane dispersion was then added to the MXene/PEDOT:PSS dispersion prepared above and vortexed for 3 h at room temperature. Then, the composite spinning solution was sonicated for 5 min, degassed, and stored until further use. The optimized mass ratio of MXene, PEDOT:PSS, and polyrotaxane was 100:20:7. The MXene/polyrotaxane/PEDOT:PSS spinning solution (1 mL) was added to a 3 mL syringe (Becton Dickinson), to which a 90° curved blunt needle (26 G) was attached. The coagulation bath and spinning conditions for PPM fiber were the same as those employed for the pure MXene fibers. The as-span fibers were collected on reels and soaked in a washing and crosslinking bath (CDI/DMSO solution with 2.27 wt% CDI) for 30 min at 60 °C, followed by soaking in a methanol solution for 20 min at room temperature. The resulting fibers were subsequently passed through a a hot-press machine at 70 °C. The axial pressure applied to the fibers was adjusted by changing the pressure of the hot-press mold from 0 kPa to 8 kPa. The optimized hot-pressing pressure was 0.2 kPa. Finally, the fibers were collected and placed in a glove box for 12 h before use.

Fabrication of A-PPM fiber

The as-prepared PPM fiber was soaked in an ethanol bath containing 1 wt% AgNWs for 10 min, followed by removing and drying at 40 °C for 10 min. This coating-drying process can be repeated to further improve the electrical conductivity of the A-PPM fiber.

Fabrication of Pressure-FS

First, 6 strands of A-PPM fibers were prepared, and every three fibers were twisted into one fiber bundle using a twisting equipment. Subsequently, each fiber bundle was coated with a thin layer of 32% waterborne polyurethane as a dielectric. Finally, the Pressure-FS was obtained by twisting together two fiber bundles coated with polyurethane into one fiber bundle.

Fabrication of Temperature-FS

First, 40 mg of PEO (M_w = 1.5 kg/mol) and 8 mg of PEO (M_w = 1.0 kg/mol) were added to 1 mL deionized water to form a PEO solution (48 mg/mL) for later use. Subsequently, three A-PPM fibers were twisted together into one fiber bundle using a twisting apparatus. The fiber bundle was twisted in the PEO solution for 2 min, followed by extraction and air drying. Then, the fiber bundle was immersed in a 15% waterborne polyurethane solution for 30 s, and the fiber bundle was suspended vertically for natural air drying to form a Temperature-FS.

Fabrication of smart wristband

The fabrication of the wearable textile wristband involved two main steps: weaving functional fibers and stitching with a self-adhesive Velcro buckle. First, to craft the functional plain-woven textiles, commercial nylon fibers were secured along the warp direction of the knitting machine, followed by interweaving the nylon fibers and the fiber sensors along the weft direction. To prepare textiles with different weft densities, the warp density was maintained at approximately 7 nylon fibers per inch. The resulting functional plain-woven textiles measured 8 cm in length and 2 cm in width, with a 0.5 cm spacing between the Pressure-FS and Temperature-FS. Then, the acquired functional textile was stitched together with a commercially available

self-adhesive Velcro buckle. This can be accomplished through manual sewing or by using a sewing machine. The obtained wristband was then assembled with a PCB and a battery to complete the fabrication of smart wristband.

Ethical approval

All experiments were performed according to the university guidelines (The Ethics Guidelines for Research Involving Human Subjects or Human Tissue from Nankai University, Nankai University Institutional Review Board, 201990). The evaluation of the wearable smart wristband for human participants followed all the ethical regulations according to the protocol above. To avoid introducing bias due to gender and age differences, participants (aged 20–30 years) were recruited from Nankai University through posted advertisements. All participants gave written informed consent before participation in the study.

Reporting summary

Further information on research design is available in the Nature Portfolio Reporting Summary linked to this article.

Data availability

The data that support the findings of this study are available from the corresponding authors upon request. Source data are provided with this paper.

References

1. Li, W. et al. Ultrastrong MXene film induced by sequential bridging with liquid metal. *Science* **385**, 62–68 (2024).
2. Mohammadi, A. V. et al. The world of two-dimensional carbides and nitrides (MXenes). *Science* **372**, eabf1581 (2021).
3. Qin, Z. et al. Recent advances in flexible pressure sensors based on MXene materials. *Adv. Mater.* **36**, 2312761 (2024).
4. Zhou, T. et al. Ultra-compact MXene fibers by continuous and controllable synergy of interfacial interactions and thermal drawing-induced stresses. *Nat. Commun.* **13**, 4564 (2022).
5. Gu, J. et al. Extremely robust and multifunctional nanocomposite fibers for strain-unperturbed textile electronics. *Adv. Mater.* **35**, 2209527 (2023).
6. Eom, W. et al. Large-scale wet-spinning of highly electroconductive MXene fibers. *Nat. Commun.* **11**, 2825 (2020).
7. Li, S. et al. Assembly of nanofluidic MXene fibers with enhanced ionic transport and capacitive charge storage by flake orientation. *ACS Nano* **15**, 7821–7832 (2021).
8. Xu, Z. et al. Ultrastiff and strong graphene fibers via full-scale synergetic defect engineering. *Adv. Mater.* **28**, 6449–6456 (2016).
9. Mao, L. et al. Stiffening of graphene oxide films by soft porous sheets. *Nat. Commun.* **10**, 3677 (2019).
10. Guo, F. et al. Hydration-responsive folding and unfolding in graphene oxide liquid crystal phases. *ACS Nano* **5**, 8019–8025 (2011).
11. Shin, H. et al. Highly electroconductive and mechanically strong $Ti_3C_2T_x$ MXene fibers using a deformable MXene gel. *ACS Nano* **15**, 3320–3329 (2021).
12. Zhou, T. et al. Interlocking-governed ultra-strong and highly conductive MXene fibers through fluidics-assisted thermal drawing. *Adv. Mater.* **35**, 2305807 (2023).
13. Wan, S. et al. High-strength scalable MXene films through bridging-induced densification. *Science* **374**, 96–99 (2021).
14. Lee, D. et al. Ultrahigh strength, modulus, and conductivity of graphitic fibers by macromolecular coalescence. *Sci. Adv.* **8**, eabn0939 (2022).
15. Xin, G. et al. Highly thermally conductive and mechanically strong graphene fibers. *Science* **349**, 1083–1087 (2015).
16. Eom, W. et al. Carbon nanotube-reduced graphene oxide fiber with high torsional strength from rheological hierarchy control. *Nat. Commun.* **12**, 396 (2021).
17. Shao, Z. & Vollrath, F. Materials: surprising strength of silkworm silk. *Nature* **418**, 741 (2002).
18. Li, J. et al. Spider silk-inspired artificial fibers. *Adv. Sci.* **9**, 2103965 (2022).
19. Chen, P. Y. et al. Comparison of the structure and mechanical properties of bovine femur bone and antler of the North American elk (Cervus elaphus canadensis). *Acta Biomater.* **5**, 693–706 (2009).
20. Yuan, S. et al. In situ experimental study on the synergistic strengthening and toughening mechanisms of multiple pore structures in deer antler. *Mater. Des.* **224**, 111306 (2022).
21. Krauss, S. et al. Inhomogeneous fibril stretching in antler starts after macroscopic yielding: Indication for a nanoscale toughening mechanism. *Bone* **44**, 1105–1110 (2009).
22. Launey, M. E. et al. Mechanistic aspects of the fracture toughness of elk antler bone. *Acta Biomater.* **6**, 1505–1514 (2010).
23. Yuan, Y. et al. Stretchable, rechargeable, multimodal hybrid electronics for decoupled sensing toward emotion detection. *Nano Lett.* **25**, 5220–5230 (2025).
24. Lee, D. & Bae, J. Soft multimodal sensors with decoupled multimodality and minimal wiring for wearable systems. *Adv. Funct. Mater.* **34**, 2409841 (2024).
25. Zhang, X. et al. Flexible temperature sensor with high reproducibility and wireless closed-loop system for decoupled multimodal health monitoring and personalized thermoregulation. *Adv. Mater.* **36**, 2407859 (2024).
26. Kim, S. et al. Purification of PEDOT:PSS by ultrafiltration for highly conductive transparent electrode of all-printed organic devices. *Adv. Mater.* **28**, 10149–10154 (2016).
27. Jiang, Y. et al. Topological supramolecular network enabled high-conductivity, stretchable organic bioelectronics. *Science* **375**, 1411–1417 (2022).
28. Zhou, T. et al. Super-tough MXene-functionalized graphene sheets. *Nat. Commun.* **11**, 2077 (2020).
29. Choi, S., Kwon, T. W., Coskun, A. & Choi, J. W. Highly elastic binders integrating polyrotaxanes for silicon microparticle anodes in lithium ion batteries. *Science* **357**, 279–283 (2017).
30. Li, L. et al. Direct-ink-write 3D printing of programmable micro-supercapacitors from MXene-regulating conducting polymer inks. *Adv. Energy Mater.* **13**, 2203683 (2023).
31. Lee, S. H. & Gleason, K. K. Enhanced optical property with tunable band gap of cross-linked PEDOT copolymers via oxidative chemical vapor deposition. *Adv. Funct. Mater.* **25**, 85–93 (2015).
32. Tian, M. et al. Designer cathode additive for stable interphases on high-energy anodes. *J. Am. Chem. Soc.* **144**, 15100–15110 (2022).
33. Shi, X. et al. Bioinspired ultrasensitive and stretchable MXene-based strain sensor via nacre-mimetic microscale "brick-and-mortar" architecture. *ACS Nano* **13**, 649–659 (2019).
34. Hou, Y. Z. et al. Strengthening and toughening hierarchical nanocellulose via humidity-mediated interface. *ACS Nano* **15**, 1310–1320 (2021).
35. Zhang, J. et al. Highly conductive $Ti_3C_2T_x$ MXene hybrid fibers for flexible and elastic fiber-shaped supercapacitors. *Small* **15**, 1804732 (2019).
36. Kong, Z. et al. Biomimetic ultratough, strong, and ductile artificial polymer fiber based on immovable and slidable cross-links. *Nano Lett.* **23**, 6216–6225 (2023).
37. Shi, H. H. et al. Sustainable electronic textiles towards scalable commercialization. *Nat. Mater.* **22**, 1294–1303 (2023).
38. Guan, F. et al. Silver nanowire–bacterial cellulose composite fiber-based sensor for highly sensitive detection of pressure and proximity. *ACS Nano* **14**, 15428–15439 (2020).
39. Xu, Z., Liu, Z., Sun, H. & Gao, C. Highly electrically conductive Ag-doped graphene fibers as stretchable conductors. *Adv. Mater.* **25**, 3249–3253 (2013).

40. Agnarsson, I., Kuntner, M. & Blackledge, T. A. Bioprospecting finds the toughest biological material: extraordinary silk from a giant riverine orb spider. *Plos One* **5**, e11234 (2010).
41. Yarger, J. L., Cherry, B. R. & van der Vaart, A. Uncovering the structure-function relationship in spider silk. *Nat. Rev. Mater.* **3**, 18008 (2018).
42. Zhu, H. et al. Direct synthesis of long single-walled carbon nanotube strands. *Science* **296**, 884–886 (2002).
43. Zhang, Y. et al. Bioinspired supertough graphene fiber through sequential interfacial interactions. *ACS Nano* **12**, 8901–8908 (2018).
44. Gosline, J. M., Guerette, P. A., Ortlepp, C. S. & Savage, K. N. The mechanical design of spider silks: From fibroin sequence to mechanical function. *J. Exp. Biol.* **202**, 3295–3303 (1999).
45. Hou, H. et al. Electrospun polyacrylonitrile nanofibers containing a high concentration of well-aligned multiwall carbon nanotubes. *Chem. Mater.* **17**, 967–973 (2005).
46. Xia, W. J., Ruiz, L., Pugno, N. M. & Keten, S. Critical length scales and strain localization govern the mechanical performance of multilayer graphene assemblies. *Nanoscale* **8**, 6456–6462 (2016).
47. Xia, W., Song, J. K., Meng, Z. X., Shao, C. & Keten, S. Designing multilayer graphene-based assemblies for enhanced toughness in nacre-inspired nanocomposites. *Mol. Syst. Des. Eng.* **1**, 40–47 (2016).
48. Zhao, X. et al. Soft fibers with magnetoelasticity for wearable electronics. *Nat. Commun.* **12**, 6755 (2021).
49. Chen, F. et al. Exploring large ductility in cellulose nanopaper combining high toughness and strength. *ACS Nano* **14**, 11150–11159 (2020).
50. Chen, C. et al. Functional fiber materials to smart fiber devices. *Chem. Rev.* **123**, 613–662 (2022).
51. Wang, L. et al. Application challenges in fiber and textile electronics. *Adv. Mater.* **32**, 1901971 (2020).
52. Fang, W. et al. Organic-inorganic covalent-ionic molecules for elastic ceramic plastic. *Nature* **619**, 293–299 (2023).
53. Wang, L., Zhang, F., Liu, Y. & Leng, J. Shape memory polymer fibers: materials, structures, and applications. *Adv. Fiber Mater.* **4**, 5–23 (2022).
54. Xiang, C. et al. Large flake graphene oxide fibers with unconventional 100% knot efficiency and highly aligned small flake graphene oxide fibers. *Adv. Mater.* **25**, 4592–4597 (2013).
55. Vilatela, J. J. & Windle, A. H. Yarn-like carbon nanotube fibers. *Adv. Mater.* **22**, 4959–4963 (2010).
56. Sasikala, S. P. et al. Graphene oxide liquid crystals: a frontier 2D soft material for graphene-based functional materials. *Chem. Soc. Rev.* **47**, 6013–6045 (2018).
57. Choi, C. et al. Twistable and stretchable sandwich structured fiber for wearable sensors and supercapacitors. *Nano Lett.* **16**, 7677–7684 (2016).
58. Qin, J. et al. Flexible and stretchable capacitive sensors with different microstructures. *Adv. Mater.* **33**, 2008267 (2021).
59. Wu, J. et al. Highly sensitive temperature-pressure bimodal aerogel with stimulus discriminability for human physiological monitoring. *Nano Lett.* **22**, 4459–4467 (2022).
60. Jeon, J., Lee, H. B. R. & Bao, Z. Flexible wireless temperature sensors based on Ni microparticle-filled binary polymer composites. *Adv. Mater.* **25**, 850–855 (2013).
61. Kireev, D. et al. Continuous cuffless monitoring of arterial blood pressure via graphene bioimpedance tattoos. *Nat. Nanotechnol.* **17**, 864–870 (2022).
62. IEEE Engineering in Medicine and Biology Society. *IEEE Standard for Wearable , Cuffless Blood Pressure Measuring Devices IEEE Engineering in Medicine and Biology Society. IEEE Std* 1708-2014 (2014).
63. Liu, Y. et al. Tailoring silver nanowire nanocomposite interfaces to achieve superior stretchability, durability, and stability in transparent conductors. *Nano Lett.* **22**, 3784–3792 (2022).
64. Liu, Y. et al. Biomimetic printable nanocomposite for healable, ultrasensitive, stretchable and ultradurable strain sensor. *Nano Energy* **63**, 103898 (2019).

Acknowledgements

This work reported here was supported the National Key R&D Program of China (2022YFA1203304), the National Natural Science Foundation of China (52173238, 61871240, 12232016, and 12172346), the Municipal Natural Science Foundation of Tianjin (20JCJQJC00010), the Youth Innovation Promotion Association CAS (2022465), the USTC Tang Scholar, and the Fundamental Research Funds for the Central Universities (WK2090000087). The numerical calculations have been done on the supercomputing systems in the Supercomputing Center of University of Science and Technology of China and in the Hefei Advanced Computing Center.

Author contributions

J.J.L. and J.F.G. conceived the idea and designed the experiments. J.J.L. and Z.Y. supervised the research project. J.F.G., D.H.L., Y.C.R., X.W.L., X.Y.J., X.L., W.Q.Z., X.L.Z., H.H.W. and X.M.Z. conducted the experiments. Y.B.Z., J.H.L., Q.W. and H.-A.W. performed the mechanical simulations and analyzations. All authors contributed to experiments and data analysis. J.J.L., J.F.G. and Y.S.C. wrote the manuscript. All authors analyzed and discussed the results.

Competing interests

The authors declare no competing interests.

Additional information

Supplementary information The online version contains supplementary material available at https://doi.org/10.1038/s41467-025-64647-w.

Correspondence and requests for materials should be addressed to YinBo Zhu, Zhao Yue or Jiajie Liang.

Peer review information *Nature Communications* thanks Huanyu Cheng, Bon-Cheol Ku, and the other, anonymous, reviewer(s) for their contribution to the peer review of this work. A peer review file is available.

Reprints and permissions information is available at http://www.nature.com/reprints

Publisher's note Springer Nature remains neutral with regard to jurisdictional claims in published maps and institutional affiliations.

Open Access This article is licensed under a Creative Commons Attribution-NonCommercial-NoDerivatives 4.0 International License, which permits any non-commercial use, sharing, distribution and reproduction in any medium or format, as long as you give appropriate credit to the original author(s) and the source, provide a link to the Creative Commons licence, and indicate if you modified the licensed material. You do not have permission under this licence to share adapted material derived from this article or parts of it. The images or other third party material in this article are included in the article's Creative Commons licence, unless indicated otherwise in a credit line to the material. If material is not included in the article's Creative Commons licence and your intended use is not permitted by statutory regulation or exceeds the permitted use, you will need to obtain permission directly from the copyright holder. To view a copy of this licence, visit http://creativecommons.org/licenses/by-nc-nd/4.0/.

© The Author(s) 2025